POLITECNICO DI TORINO
Repository ISTITUZIONALE

Thermal stress analysis of variable angle tow composite plates through high-order structural models

Terms of use:

(Article begins on next page)

11 February 2024

Thermal stress analysis of variable angle tow composite plates through high-order structural models

A. Pagani *, E. Zappino, F. Bracaglia, R. Masia, E. Carrera

Mul2 Lab, Department of Mechanical and Aerospace Engineering, Politecnico di Torino, Corso Duca degli Abruzzi 24, 10129 Torino, Italy

ARTICLE INFO

ABSTRACT

This work focuses on thermo-elastic analysis of Variable Angle Tow (VAT) composite plates. Emphasis is given to the through-the-thickness 3D stress component distributions as a consequence of constant temperature profiles. High-order structural models are used, in order to take into account the volumetric and the distortion contributions. The last contribute arise from boundary conditions or asymmetric staking sequences. Governing equations of the uncoupled thermo-elastic problem are derived in the domain of the Carrera Unified Formulation (CUF), which in turn is coupled with a classical finite element method to obtain opportune numerical solutions. The advantage of using CUF lies in the fact that different theories of structures can be implemented automatically and a critical study on the use of standard to high-order plate finite elements can be performed with ease. In this manner we classify models based on their efficiency and depending on the degree of accuracy needed, both in terms of displacements and stresses. Different numerical problems are considered and it is demonstrated that layerwise approximations are needed whenever shear stresses trends are of interest. Boundary Conditions influence more the choice of the adequate expansion theory otherwise.

1. Introduction

The thermal response of a structure holds significant importance across various aerospace applications, particularly when employing composite materials. The present work describes the thermal stresses arising along Variable Angle Tow (VAT) composite plates. High-order structural models are used to describe various plate configurations subjected to a constant thermal profile.

Composite materials are central to the aerospace, mechanical, civil, and automotive industries. Their high strength-to-weight ratio and stiffness properties make them appealing. They offer a wide range of thermal applications, which can be customized by selecting the appropriate material for the matrix. This flexibility, combined with the possibility of negative thermal expansion coefficients, favors the choice of composite materials for numerous applications. Design and production flexibility are other factors that have contributed to the high popularity of composite materials. In fact, they have the capability to be tailored in the various deposition directions [1]. New advanced composite materials have been developed in recent years, increasing their tailoring flexibility. It is now possible to exploit new deposition technology such as the Automated Fibre Placement (AFP) technique [2] and the Continuous Tow Shearing (CTS) process [3]. Variable Angle Tow (VAT) composites have gained considerable attention due to their

unique fiber deposition capabilities. By allowing fibers to follow curvilinear paths, VAT plates offer increased degrees of freedom and the potential for enhanced structural performance.

Hyer and Charette [4] first proposed the idea of fibers with curved trajectories in the early 1990s, which was limited until then by technological and manufacturing constraints. In the year that followed, VAT plates and shells were studied extensively. For instance, Demasi et al. [5] investigated the stress distribution of VAT plates employing Equivalent Single Layer (ESL) and Layer Wise (LW) theories, and Patni et al. [6] provide accurate VATs 3D stress fields description. VATs were frequently studied to adapt the fiber deposition to the structure behavior. Using VAT reinforcement around the hole, Zhu et al. [7] investigated the increase in the ultimate strength of the open-hole specimen. The optimization of the fiber deposition path to increase the critical buckling load has also been studied with different methods [8–10]. Curved fiber deposition increases production complexity and, consequently, the eventuality of unexpected phenomena or manufacturing errors such as misalignments. Groh et al. [11] provide non-intuitive localized stress fields in tow-steered laminates far from any boundaries. Pagani et al. [12,13] and Sanchez-Majano et al. [14] studied the effect of manufacturing defects on the in-plane normal stresses, failure, and buckling. The advantages of using VAT composites

under a mechanical load are clearly established in numerous works emphasizing the influence of curved deposition on stiffness improvement [15,16]. Additionally, the influence of external fields has been investigated for VAT composite structures since they can cause abrupt failures or unexpected changes in shape. As a consequence, the buckling critical load due to constant thermal profile is investigated by Duran et al. [17] and Vescovini et al. [18] for VAT symmetrically balanced laminates.

Structures are subjected to different external environments, which act as additional loads. Usually, the thermal environment is particularly critical and intense in the case of spacecraft and high-speed aircraft. This thermal load can be due to various factors, such as solar radiation and drag or, in the case of composite materials, the manufacturing process.

Different methods have been developed to describe the thermal influence on structures and materials. In [19], beams, plates, and shells-based solutions are developed through the theory of elasticity for thermal bending, determining the applicability of the various laminate models, three-dimensional (3D) exact solutions are also reported in [20]. Other studies investigated the influence of thermal loads on the variation of natural frequencies and critical buckling load [21,22]. Moreover, a review of the thermal buckling for plates and shells is reported in [23], where the rule of the thermal properties is discussed. Additionally, Kant and Khare [24] describe studies involving thermo-elastic behavior using classical or first-order theories. However, the traditional plate theories are often insufficient when considering thermal loads. On the other hand, although accurate, using three-dimensional (3D) elements results in a higher computational cost.

Many works on improved plate and shell models are addressed in the literature for thermo-elasticity problems. However, most papers do not consider refined approximation of the out-of-plane displacements. Volumetric deformations are important in the case of thermal load, and out-of-plane normal stress must be considered. Recent studies have focused on developing higher-order 2D models, which provide a more accurate representation of the thermal response. Precise models for describing normal and shear stresses are developed through the post-processing technique in [25]. Several higher-order two-dimensional (2D) models have been developed recently. Among these models, the thermal problem is investigated by Whu and Chen [26] through the higher-order model and by Han et al. [27] using the enhanced first-order shear deformation theory. Carrera [28] investigated the impact of the through-the-thickness temperature profile on the thermo-mechanical behavior of multilayered anisotropic thick and thin plates. The trend of thermal stresses has also been studied over the years for plates made of isotropic material [29] and straight-fiber laminate [30]. The influence of the thermal profile is also established in [31], where thermal and mechanical boundary conditions, body forces, and heat sources are considered in the most general forms. Furthermore, in [32], the thermo-elastic static analysis of multilayered shell structure is performed within the Carrera Unified Formulation framework using Equivalent Single Layer (ESL) models, Layer Wise (LW) models, and variable-kinematic models. The use of laminated materials in the field of structure analysis introduces new numerical challenges. The classical theories developed for the one-layered structures need to be revised to describe the discontinuity of mechanical and physical properties along the thickness due to the multi-layers [33]. As a result, many theories have been developed to explain how displacements, strains, and stresses behave along thickness. The ESL, LW [34], and Zig-Zag (ZZ) [35] hypotheses are among those that have received the most attention. Different works have been published during the years to evaluate the better model for each case of study [5,9,18,25,30,36,37].

In this work, the CUF is employed to explore complete and high-order structural models to opportunely describe the intricate nature of the thermo-elastic coupling in laminated structures. Particular emphasis is given to VAT structures whose anisotropy further enhance the coupling between the in-plane and out-of-plane mechanics. The CUF

is exploited within the finite element method, which makes it possible to describe displacement fields with significantly lower computational costs than 3D modeling. The main advantages of employing CUF are linked to the accurate and formally invariant implementation of the multifield unknowns and the different high-order kinematic theories.

This work provides an accurate description of thermal stress trends that develop along the thickness of VAT composite plates with a focus on the influence of the accuracy of the adopted expansion theory. To the best of the authors knowledge, no results of thermal stresses inherent to VAT plates are available to date. The behavior of VAT composites may differ from that of conventional materials, as these have a greater anisotropy due to the curvature of the fiber. Nevertheless, this anisotropy is particularly important in the thermal properties, which may differ from that of straight-fiber material. As a consequence, we found that VAT behave quite differently in a thermal environment if compared to classical composites. This generally justifies the need for additional studies on VAT laminates by higher order theories.

The manuscript is organized in the following sections: Section 2 reports the VAT numerical description employed in the present work, specifying the rotation approach necessary for variable orientation description. Section 3 is focused on the mathematical characterization of the thermo-mechanical problem through the CUF. In Section 4, some numerical results are reported for different cases of interest. Last, some overall considerations are presented in Discussion 5 and Conclusions 6.

2. Variable Angle Tow (VAT) notation and geometrical description

In the present study, VAT plates are analyzed utilizing plate elements. VATs refer to advanced composite materials incorporating fibers following a curvilinear path to enhance efficiency. This curvilinear path enables the adjustment of composite properties, such as stiffness and strength, to meet specific requirements based on the lamination and boundary conditions. Therefore, employing a curvilinear path makes it possible to act on more degrees of freedom and align the fiber orientation to specific local requirements. Additionally, a curvilinear path results in varying fiber orientation angles between different points, leading to distinct local material properties. Usually, the deposition of the curved fibers employing the presented techniques results in manufacturing defects such as gap areas or thickness variations [38]. Although they are not considered in the present research, defects may affect the mechanical performance of VAT structures and optimal design [12–14]. When a linear fiber angle variation over the lamina is considered, the orientation of the fibers can be described by Eq. (1) through the notation provided by Guardal et al. in [39]:

$$\theta(x') = \Phi + T_0 + \frac{T_1 - T_0}{d}|x'| \tag{1}$$

where Φ indicates the rotation of the local reference system with respect to a specific reference direction. x' is the coordinate of the new rotate system, and T_0 and T_1 are two different reference angles with a characteristic distance named with d which is equal to $a/2$ when Φ is $0°$ and $b/2$ when Φ is $90°$.

Fig. 1(a) shows the fiber deposition representation, including all the relevant reference parameters. The new reference system is rotated with respect to the global one of the angle Φ. The fiber orientation angle is determined using the following relation $x' = x\cos(\Phi) + y\sin(\Phi)$. For the sake of clearance, an example of the deposition path is reported in Fig. 1(b) where the lamination is $[0 < 90, -45 >]$ with $\Phi = 0°$, $T_0 = 90°$, $T_1 = -45°$. Considering these parameters, the coordinate x' became $x' = x$ and the distance d is equal to the edge $a/2$. Substituting the numerical value in Eq. (1) the orientation of the fiber is $\theta(x') = \theta(x) = 0 + 90 + \frac{(-45-90)}{a/2}|x| = 90 - \frac{135}{a/2}|x|$. The presence of VATs implies that the rotation of the lamina is not allowed with a single rotation matrix, as in a straight configuration. Thus, a different rotation strategy must be employed, depending on the local fiber orientation. The methodology employed in the present investigation evaluates the
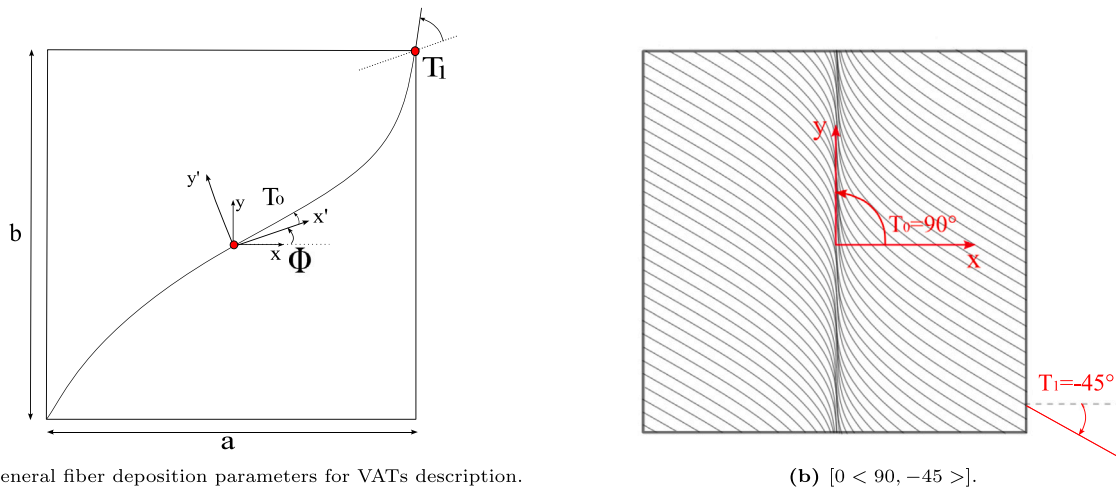
(a) General fiber deposition parameters for VATs description.

(b) $[0 < 90, -45 >]$.

Fig. 1. Variable Angle Tow (VAT) representation.

material coefficients of the VAT structure at specific Gauss points [40]. This Gauss evaluation approach differs from the orientation definition employed in the commercial codes, which treat the lamination angle as constant across the entire element. As a result, the study of VAT structures is more precise and practical in the present work. This increase in accuracy is due to the evaluation in the Gauss point since the varying stiffness coefficients of the material are considered in multiple places for the same FE.

3. Thermo-mechanical decoupled model for VAT plates

3.1. Preliminary concepts

The present work investigates a steady-state thermo-mechanical problem using a decoupled approach. Primary variables are displacements which are reported in the vector below:

$$\mathbf{u}^T(x, y, z) = \begin{pmatrix} u_x & u_y & u_z \end{pmatrix} \tag{2}$$

where the apex T means transposition. The expressions of strains and stresses vector are defined respectively in Eqs. (3) and (4) in a global Cartesian reference system.

$$\boldsymbol{\varepsilon}^T = \begin{pmatrix} \varepsilon_{xx} & \varepsilon_{yy} & \varepsilon_{zz} & \varepsilon_{xz} & \varepsilon_{yz} & \varepsilon_{xy} \end{pmatrix} \tag{3}$$

$$\boldsymbol{\sigma}^T = \begin{pmatrix} \sigma_{xx} & \sigma_{yy} & \sigma_{zz} & \sigma_{xz} & \sigma_{yz} & \sigma_{xy} \end{pmatrix} \tag{4}$$

The geometrical relations reported in Eq. (5) define the linear relation between the displacements $\mathbf{u}$ and strains $\boldsymbol{\varepsilon}$:

$$\boldsymbol{\varepsilon} = \mathbf{b}\mathbf{u} \tag{5}$$

where $\mathbf{b}$ is a 6×3 linear differential operator whose explicit form is reported in Appendix A. Further details about the geometrical relations and their operator are available in [41]. The stress vector $\boldsymbol{\sigma}$ is defined by the Hooke law through the material constitutive matrix $\tilde{\mathbf{C}}(x, y)$.

$$\boldsymbol{\sigma} = \tilde{\mathbf{C}}(x, y)\boldsymbol{\varepsilon} \tag{6}$$

Where $\tilde{\mathbf{C}}$ is defined in the Cartesian global reference system through the Eq. (7) acting on the matrix of the material properties $\mathbf{C}$ which is in the material reference system and whose form is reported in Eq. (9).

$$\tilde{\mathbf{C}}(x, y) = \mathbf{T}(x, y)\mathbf{C}\mathbf{T}^T(x, y) \tag{7}$$

The rotation matrix $\mathbf{T}$ is the local rotation matrix describing the relation between material reference system and element reference system. This matrix is a function of the lamination angle and it is equivalent

between VAT and classical straight-fiber composites reported in [42]. Nevertheless, as θ varies point-wise within the single ply in the case of VAT, is becomes clear that $\mathbf{T}(x, y)$. When simulating VAT structures by commercial FE software, it is straightforward to consider the lamination constant within the element, which eventually assumes a linear distribution of the problem unknowns within the computational domain. This approach definitely affects the numerical effectiveness of the mathematical model, whose convergence is no more a function of the mere element size and polynomial order, but also will be affected by the steering gradient within the element. This is not the case in the model proposed in this work, where the lamination angle is evaluated at each Gauss point within the single high order finite element [40]. This ensures a more precise and practical description with multiple evaluations of the local properties of each finite element. In contrast, traditional approaches employ a constant rotation for each finite element which requires a more refined mesh to adequately capture the orientation description.

It is worthwhile to decompose strain and stress into the sum of mechanical and thermal components to describe the decoupled thermo-mechanical problem. These two components are distinguished by different subscripts, where subscript m represents the mechanical component, and the subscript ϑ corresponds to the thermal component.

$$\boldsymbol{\sigma} = \tilde{\mathbf{C}}\boldsymbol{\varepsilon} = \tilde{\mathbf{C}}\left(\boldsymbol{\varepsilon}_m + \boldsymbol{\varepsilon}_\vartheta\right) = \tilde{\mathbf{C}}\boldsymbol{\varepsilon}_m - \tilde{\lambda}\theta = \boldsymbol{\sigma}_m + \boldsymbol{\sigma}_\vartheta \tag{8}$$

In the given equations, θ indicates applied over-temperature, while $\boldsymbol{\alpha}$ represents the thermal expansion coefficient. The stresses-temperature coefficient defined in the global reference system is denoted by $\tilde{\lambda}$, which couples the two fields. To obtain $\tilde{\lambda}$ the rotation matrix is applied as shown in Eq. (11) to $\lambda = \mathbf{C} \cdot \boldsymbol{\alpha}$ which is defined in the material system.

The constitutive matrix $\mathbf{C}$ is presented in Eq. (9), where the material is considered orthotropic, homogeneous, and operating in the linear elastic range, Eq. (10) reports the stresses-temperature coefficient λ.

$$\mathbf{C} = \begin{pmatrix} C_{11} & C_{12} & C_{13} & 0 & 0 & 0 \\ C_{21} & C_{22} & C_{23} & 0 & 0 & 0 \\ C_{31} & C_{32} & C_{33} & 0 & 0 & 0 \\ 0 & 0 & 0 & C_{44} & 0 & 0 \\ 0 & 0 & 0 & 0 & C_{55} & 0 \\ 0 & 0 & 0 & 0 & 0 & C_{66} \end{pmatrix} \tag{9}$$

$$\boldsymbol{\lambda}^T = \{\lambda_1 \quad \lambda_2 \quad \lambda_3 \quad 0 \quad 0 \quad 0\} \tag{10}$$

$$\tilde{\lambda} = \lambda \mathbf{T}^T \tag{11}$$

3.2. Unified theory of plate structures

When compared to the conventional model, such as Classical Lamination Theory (CLT) or First-order Shear Deformation Theory (FSDT), Higher-Order Theories (HOTs) models offer increased accuracy in solutions. The Carrera Unified Formulation (CUF) is an efficient framework that describes all the kinematic models from classical to high-order theories. The present study employs the CUF to implement the high-order theories, enabling the description of models using different expansion orders. The approach is based on a condensed notation that expresses the displacement fields in terms of base functions with arbitrary forms and orders. This condensed notation can represent all kinematic theories and allows the definition of the Fundamental Nuclei (FNs) of the problem.

Furthermore, the CUF formulation enables the automatic implementation of a multi-field load with minimal changes to the pure mechanical field. This implementation enables accurate 2D multi-field description, taking advantage of unlimited unknowns per node. Further details about the CUF framework and its implementation can be found in Ref. [43].

Using the CUF, the 3D displacement field $u(x, y, z)$ can be represented by adopting a refined two-dimensional kinematic model. This model incorporates the contribution of $F_\tau(z)$ and $u_\tau(x, y)$. Here, $F_\tau(z)$ represents arbitrary expansion functions that describe the displacement behavior along the thickness, and $u_\tau(x, y)$ denotes the generalized displacement, which represents the solution in the plane of the plate:

$$u(x, y, z) = F_\tau(z)u_\tau(x, y) \quad \tau = 1, 2, \ldots, N \tag{12}$$

where τ ranges from 1 to N, representing the number of expansion terms, and the double indices indicate a summation.

In order to approximate the unknowns vector, the problem is solved using the Finite Element Method (FEM) as shown in Eq. (13). This method involves introducing shape functions N_i and the nodal unknowns q_i:

$$u(x, y, z) = F_\tau(z)N_i(x, y)q_{\tau i} \tag{13}$$

where i denotes the number of nodes of the plate element. By combining these approximations, the CUF-FEM approach allows for an efficient and accurate solution to the problem at hand.

Due to their "transversely anisotropy", employing a two-dimensional model, new challenges arise in describing material properties along the thickness of multilayered structures. In laminated structures, different layers lead to transverse discontinuous mechanical properties, and the interfaces between layers result in abrupt changes and varying slopes in displacement profiles. As a result, the in-plane stress components may be discontinuous at the interface, while the transverse stresses must remain continuous at each interface. These requirements are referred to as Interlaminar Continuity (IC) [43]. Simply improving the polynomial order of expansion may not guarantee compliance with continuity conditions and the correct representation of the change in the slope of displacements in the case of high transverse anisotropy. Consequently, various approaches have been developed to describe the laminate material properties, with the most common ones being the Equivalent Single Layer theory (ESL) and Layer Wise theory (LW).

In the ESL approach, the stiffness matrix of the entire plate is obtained by homogenizing the constitutive properties of the individual layer. The behavior of the multilayer is then analyzed as that of a single-layer plate, characterized by the same variables assumed for the entire cross-section. Material properties are defined by direct addiction of the properties from every single layer creating a new homogeneous material. The ESL approach is "kinematically homogeneous" and is not sensitive to the individual layers. However, it can describe transverse shear and normal strains.

On the other hand, the LW approach imposes continuity at every interface with the description of each layer by its unique set of variables expanded on the thickness direction. Fig. 2 shows a graphical representation of the ESL and LW FNs.

Several functions can be used as F_τ describing the in-thickness expansion. In this study, it is presented an investigation of the use of Lagrange Expansion (LE) with the LW approach and Taylor Expansion (TE) adopting ESL theory. TE models are based on polynomial expansion functions that describe the displacement along the thickness, allowing for arbitrary increases in order. The linked displacement remains continuous through the layers and is defined by the nodes placed on a reference surface. On the contrary, LE models are based on Lagrange polynomials, where the unknowns of the problem are the pure displacement components, and the nodes can be defined along the thickness. Different orders of LE can be used, and each order allows for the imposition of Boundary Conditions (BCs) at each interface of the multilayer. Further details about the LE and TE expansion models and functions can be found in [41,44] respectively.

3.3. Thermo-mechanical problem

The variational principles allow us to write the governing equation and the relative BCs of the problem. In the present work, the Principle of Virtual Displacements (PVD) is employed to obtain the description of the multifield problem. Given a set of admissible configurations, the balanced configuration is only achieved when the equality of internal and external virtual work is satisfied, as reported in Eq. (14):

$$\delta L_{int} = \delta L_{ext} \tag{14}$$

where the symbol δ denotes the virtual variation, L_{int} stands for the strain energy, and L_{ext} is the work of the external loads. When a decoupled approach is adopted, the temperature is imposed at each interface as a known value since it is not an unknown of the problem. The derivation of the internal work is reported in Eq. (15):

$$\delta L_{int} = \int_V \delta \boldsymbol{\varepsilon}_m^T \boldsymbol{\sigma} dV = \int_V \delta \boldsymbol{\varepsilon}_m^T \left(\boldsymbol{\sigma}_m + \boldsymbol{\sigma}_\vartheta \right) dV = \int_V \delta \boldsymbol{\varepsilon}_m^T \left(\tilde{\boldsymbol{C}} \boldsymbol{\varepsilon}_m - \theta \tilde{\boldsymbol{\lambda}} \right) dV$$

$$= \int_V \delta \boldsymbol{\varepsilon}_m^T \tilde{\boldsymbol{C}} \boldsymbol{\varepsilon}_m dV - \int_V \delta \boldsymbol{\varepsilon}_m^T \theta \tilde{\boldsymbol{\lambda}} dV \tag{15}$$

where V is the plate volume. Introducing CUF and FEM as explained in Eqs. (12) and (13), the first term of the Eq. (15) can be explained as:

$$\int_V \delta \boldsymbol{\varepsilon}_m^T \tilde{\boldsymbol{C}} \boldsymbol{\varepsilon}_m dV = \int_V (\boldsymbol{b} \delta \boldsymbol{u})^T \tilde{\boldsymbol{C}} (\boldsymbol{b} \boldsymbol{u}) dV$$

$$= \int_\Omega \int_h \left(\boldsymbol{b} F_s(z) \delta \boldsymbol{u}_j(x, y) \right)^T \tilde{\boldsymbol{C}} \boldsymbol{b} F_\tau(z) \boldsymbol{u}_i(x, y) d\Omega dz$$

$$= \int_\Omega \int_h \left(\boldsymbol{b} F_s(z) N_j(x, y) \delta \boldsymbol{q}_{sj} \right)^T \tilde{\boldsymbol{C}} \underbrace{\boldsymbol{b} F_\tau(z) N_i(x, y)}_{\boldsymbol{B}_{\tau i}} \boldsymbol{q}_{\tau i} d\Omega dz$$

$$= \int_\Omega \int_h \delta \boldsymbol{q}_{sj}^T \boldsymbol{B}_{sj}^T \tilde{\boldsymbol{C}} \boldsymbol{B}_{\tau i} \boldsymbol{q}_{\tau i} d\Omega dz = \delta \boldsymbol{q}_{sj}^T \left(\int_\Omega \int_h \boldsymbol{B}_{sj}^T \tilde{\boldsymbol{C}} \boldsymbol{B}_{\tau i} d\Omega dz \right) \boldsymbol{q}_{\tau i} \tag{16}$$

where the volume V is divided into two parts, Ω which denotes the plate surface and h that is the plate thickness. Including CUF and FEM in the PVD, the differential operator $\boldsymbol{b}$ is applied both to the shape functions and the thickness expansion functions and, as a result, the matrix $\boldsymbol{B}$ can be defined. Using a similar procedure, the second term of Eq. (15) is obtained and reported in Eq. (17).

$$\int_V \delta \boldsymbol{\varepsilon}_m^T \theta \tilde{\boldsymbol{\lambda}} dV = \int_\Omega \int_h (\boldsymbol{b} \delta \boldsymbol{u})^T \tilde{\boldsymbol{\lambda}} \theta d\Omega dz$$

$$= \int_\Omega \int_h \left(\boldsymbol{b} F_s(z) N_j(x, y) \delta \boldsymbol{q}_{sj} \right)^T \tilde{\boldsymbol{\lambda}} \theta d\Omega dz = \int_\Omega \int_h \delta \boldsymbol{q}_{sj}^T \boldsymbol{B}_{sj}^T \tilde{\boldsymbol{\lambda}} \theta d\Omega dz \tag{17}$$

When only a thermal profile is applied as external load, the virtual external work consists of what has obtained in Eq. (17), and the PVD can be represented as in Eq. (18).

$$\delta \boldsymbol{q}_{sj}^T \underbrace{\left(\int_\Omega \int_h \boldsymbol{B}_{sj}^T \tilde{\boldsymbol{C}} \boldsymbol{B}_{\tau i} d\Omega dz \right)}_{\boldsymbol{K}^{\tau sij}} \boldsymbol{q}_{\tau i} - \delta \boldsymbol{q}_{sj}^T \underbrace{\int_\Omega \int_h \boldsymbol{B}_{sj}^T \tilde{\boldsymbol{\lambda}} \theta d\Omega dz}_{\boldsymbol{\Theta}^{sj}} = 0 \tag{18}$$
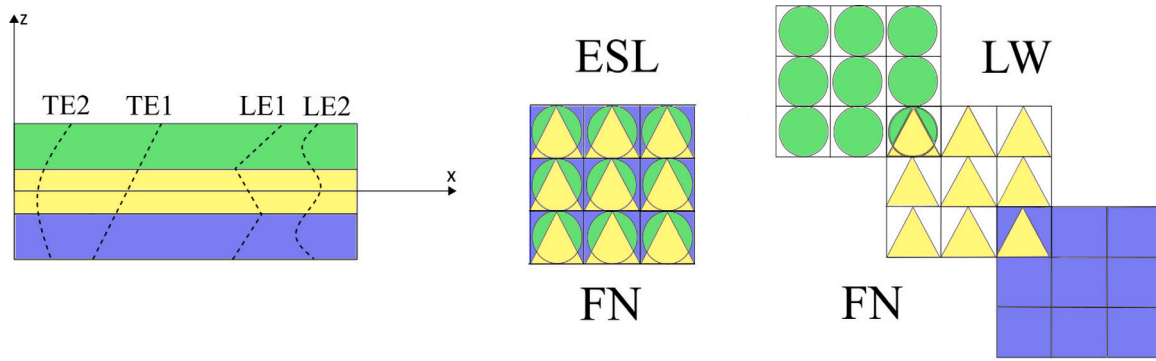
Fig. 2. Graphical representation of the Fundamental Nuclei (FNs) of the stiffness matrix for Equivalent Single Layer (ESL) and Layer Wise (LW) theories.

Through internal work, it is possible to define the fundamental nucleus of the stiffness matrix for the problem. In the decoupled approach, this nucleus is a 3 × 3 matrix, and its explicit terms are provided in Appendix B. Additionally, it is also possible to define the vector Θ, which is a 3 × 1 matrix, representing the fundamental nucleus of the thermal load matrix. Its form is determined by the thermal profile, which is constant along the thickness in this analysis. Detailed procedures for obtaining the matrix Θ are described in [30]. The governing equations shown in Eq. (19) are written using the compact notation of the fundamental nucleus. By employing the CUF building loops, these global governing equations can be automatically defined independently of the selected expansion theory.

$$\delta q_{sj} : K^{\tau sij} q_{\tau i} = \Theta^{sj} \qquad (19)$$

Where $K^{\tau sij}$ represents the Fundamental Nucleus (FN) of the stiffness matrix, the complete matrix can be assembled using four building loops: two loops are applied on the nodes governed by the indexes τ and s, and the other two loops are applied on the element, ruled by i and j. The FNs are invariant to the number of nodes and to the selected shape functions. This advantage allows an efficient implementation in a code [43].

4. Numerical results

Some thermo-mechanical analyses are carried out and reported in the following sections using the decoupled governing equations obtained within the CUF framework through the PVD. Furthermore, the best expansion theory order is investigated for every BCs and lamination case.

Each analysis is focused on the same geometry, which has equal edges that are 50 mm long and a thickness of 1 mm, as reported in Fig. 3. A constant one-degree over-temperature θ is applied across the entire plate and is regarded as an external thermal load in each analysis.

In Section 4.1, a reference analysis with a straight fiber configuration is presented and compared with ABAQUS 3D elements. After the assessment, two lamination cases are analyzed, considering both symmetric and not-symmetric stacking sequences. Notably, the asymmetric configuration produces geometrical coupling phenomena that result in out-of-plane shear stresses, which are absent in symmetric cases. In the end, in Section 5, a comparison concerning the LE and TE models is reported.

Table 1 lists Carbon Fiber Composite (CFC) and Glass Fiber Reinforced Polymer (GFRP) properties which are considered in the following studies. For each analysis, the results are taken in Point S (12.5,12.5) [mm] with the reference system located in the center of the plate. The plate analyzed in the present work presents different constraints, materials, and laminations which are reported in the following list:
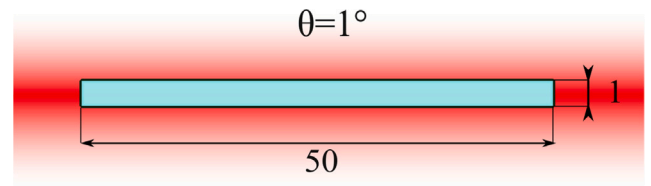

Fig. 3. Plate [mm].

- In Section 4.1, the analyzed plate is Carbon Fiber Composite (CFC) straight fiber plate with $[0/60]_s$ lamination and clamped edges, which are compared to ABAQUS results.
- In Section 4.2 the analyzed plate is Carbon Fiber Composite (CFC) symmetric VAT plate with $[0 < 90, 60 >, 0 < 45, 0 >]_s$ lamination. Fully clamped and simply supported edges are considered.
- In Section 4.3 the analyzed plate is Glass Fiber Reinforced Polymer (GFRP) asymmetric VAT plate with $[2(0 < 90, 60 >), 2(0 < 45, 0 >)]$ lamination. Fully clamped and simply supported edges are considered.

4.1. Assessment

In this section an analysis on classical straight fiber laminate is presented. The square plate is analyzed and the results are reported to evaluate the accuracy of the present model and of the applied plate theories. Moreover, the results are compared to those obtained using ABAQUS. The plate presents four layers with the same thickness, composed of CFC, whose properties are reported in Tables 1 and 2. The lamination is $[0/60]_s$ and is reported in Fig. 4, geometry and thermal load are represented in Fig. 3. All the plate edges are clamped. A convergence analysis varying the number of bi-quadratic nine nodes Q9 plate elements is reported in Table 3 and depicted in Fig. 5. While the impact of the theory order on the plate analysis using different orders of TE and LE models in-thickness expansion is investigated in Table 4 and reported in Fig. 6.

ABAQUS reference results are obtained using 3D linear elements. The results are taken in Point S (12.5,12.5) [mm] with the reference system located in the center of the plate.

According to the results reported in Table 3 and Fig. 5, the 22 × 22 Q9 is selected to ensure a satisfactory convergence trend while minimizing the computational cost.

Figs. 5 and 6 report the calculated in-plane stress trends and the displacement. The first and the last layers of the plate present 0° lamination angle, which causes no in-plane stress because the term λ_{12} is null. On the other hand, the central layers present in-plane shear stress due to the 60° lamina orientation. Furthermore, due to the symmetry of the staking sequence, there is no coupling between in and

Table 1
Material mechanical coefficients.

Material	E_{11}	$E_{22} = E_{33}$	$v_{12} = v_{13}$	v_{23}	$G_{12} = G_{13}$	G_{23}
Carbon Fiber Composite (CFC)	144.8 GPa	9.65 GPa	0.3	0.3	4.14 GPa	3.45 GPa
Glass Fiber Reinforced Polymer (GFRP)	48.9 GPa	5.5 GPa	0.33	0.33	2.5 GPa	2 GPa

Table 2
Material thermal coefficients.

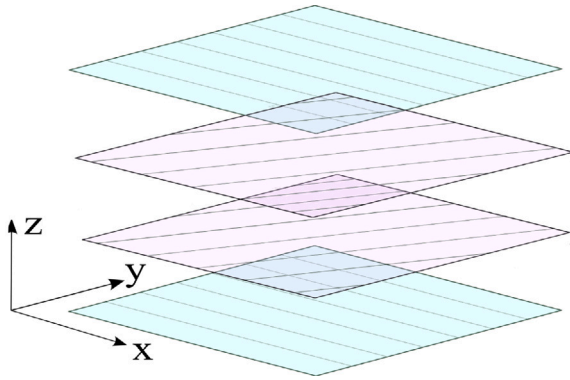| Material	α_1	$\alpha_2 = \alpha_3$
Carbon Fiber Composite (CFC)	$-0.26279 \times 10^{-6}\ C^{-1}$	$30.535 \times 10^{-6}\ C^{-1}$
Glass Fiber Reinforced Polymer (GFRP)	$3.9 \times 10^{-6}\ C^{-1}$	$49.7 \times 10^{-6}\ C^{-1}$

Fig. 4. Assessment stacking sequence [0/60/60/0].

Table 3
Convergence study changing the number of Q9 elements with expansion theory 4LE3. ABAQUS 3D analyses is reported as a reference. [0/60/60/0] CFC plate with $\theta = 1°$ and clamped edges. Results are taken at Point S. The stresses are evaluated at $z = 0$, displacement at $z = \pm h/2$.

Mesh size	$u_z \times 10^4$ [mm]	σ_{xx} [kPa]	σ_{yy} [kPa]	σ_{xy} [kPa]	DOFs
ABAQUS 3D reference					
Mesh A	±0.1994	−236.68	−117.63	103.81	25 215
Mesh B	±0.1993	−235.82	−115.45	104.65	77 760
Mesh C	±0.1992	−235.23	−113.96	105.26	606 015
Present method 4LE3					
11 × 11	±0.2007	−236.86	−118.36	103.40	20 631
22 × 22	±0.1993	−235.77	−115.32	104.70	78 975
30 × 30	±0.1993	−235.50	−114.64	104.98	145 119
38 × 38	±0.1993	−235.36	−114.28	105.12	231 231

Table 4
Investigation of the expansion theory influences with 22 × 22 Q9 in-plane mesh.[0/60/60/0] CFC plate with $\theta = 1°$ and clamped edges. Results are taken at point S with $z = \pm h/2$ for the displacement and $z = 0$ for the stresses.

Model	$u_z \times 10^4$ [mm]	σ_{xx} [kPa]	σ_{yy} [kPa]	σ_{xy} [kPa]	DOFs
ABAQUS 3D reference					
Mesh C	±0.1992	−235.23	−113.96	105.26	606 015
Present method 22 × 22 Q9					
TE1	±0.1993	−235.81	−115.44	104.65	12 150
TE2	±0.1993	−235.77	−115.34	104.69	18 225
TE3	±0.1993	−235.78	−115.35	104.69	24 300
4LE2	±0.1993	−235.77	−115.32	104.70	54 675
4LE3	±0.1993	−235.77	−115.32	104.70	78 975

out-of-plane behavior. The plate does not bend, implying out-of-plane shear stresses are not generated and not reported for the present case.

Due to the uniform thermal profile, the stress results remain constant across all individual layers. The thermal load is considered the same in every layer and along the whole layer, and the stresses are influenced by the material property, which is constant for each layer.

As clear from the graphs, the ABAQUS model results perfectly overlap the present method stresses trend. Therefore, in the case of commercial codes, 3D elements are necessary to obtain the proper description of the thermal problem along the thickness. Based on the presented findings, it is evident that TE is appropriate for the current case. In the case of ABAQUS analysis, the use of 3D elements implies an increase in the DOFs of the problem. Given the simplicity of the proposed problem, in the present method analysis, the linear Taylor expansion results are accurate and present a lower computational cost with 12 150 DOFs compared to 77 760 DOFs required in the ABAQUS analysis.

4.2. Carbon Fiber Composite symmetric VAT plate

A VAT laminated panel composed of CFC is analyzed in the present section, and the results are reported in Table 5. The lamination is symmetric, and the stacking sequence is $[0 < 90, 60 >, 0 < 45, 0 >]_s$. Geometry and material are reported in Fig. 3 and Tables 1 and 2 respectively. Fig. 7 depicts the staking sequence of the plate.

The external thermal load is not changed to the assessment and is equal to $\theta = 1°$. The plate constraints are varied studying configuration with all edges clamped (CCCC), which results are represented in Fig. 8 and with simply supported (SSSS) edges in Fig. 9. Some numerical results are collected in Table 5, and only results for TE1 and LE3 are reported for the clamped plate. As can be seen from the closeness of the reported stress values, the other expansion theories may not show significant variations in stress magnitude. Furthermore, Table 5 and Fig. 8 also compare the present results and the one obtained for a clamped plate on ABAQUS. It is clear that the results are very close and present the same trend with a minimum difference due to the difference in the orientation evaluation. Furthermore, the ABAQUS model is created using one C3D8R element for each layer of the laminate with some losses in the accuracy of the numerical model.

In Figs. 8 and 9 only σ_{yy} and σ_{xy} are represented for the different constraint conditions. Although other in-plane stresses exist for the present configuration, they have not been reported, as applying different theories did not consistently affect the stress trend. The symmetric plates do not bend, and out-of-plane stresses have not risen. The absence of bending is due to the selected thermal load and to the symmetry of the stacking sequence. In Fig. 9, the stress rising along the SSSS plates is carried over. The influence of the thickness expansion in the in-plane stresses is more evident for SSSS plate than for CCCC, and this is due to the freedom given by the simply supported configuration. Therefore, the difference in the constraint does not affect much the entity of the developed stresses that are about the same order of magnitude for the two cases. Some considerations about the best-adopted expansion theories for the present case are reported in Section 5. Still, it is clear from the reported trends that LE models are more accurate in the case of SSSS BCs.

4.3. Glass fiber reinforced asymmetric VAT plate

The present section analyzes the same plate geometry represented in Fig. 3 composed of GFRP layers. The lamination is $[2(0 < 90, 60 >), 2(0 < 45, 0 >)]$, which is reported in Fig. 10. Clamped (CCCC) and simply supported (SSSS) configurations are analyzed. The expansion theory order influence is investigated and reported in Figs. 12 and 13. The results are also listed in Tables 6 and 7. Displacement in thickness direction for SSSS and CCCC configurations is reported in Fig. 11.
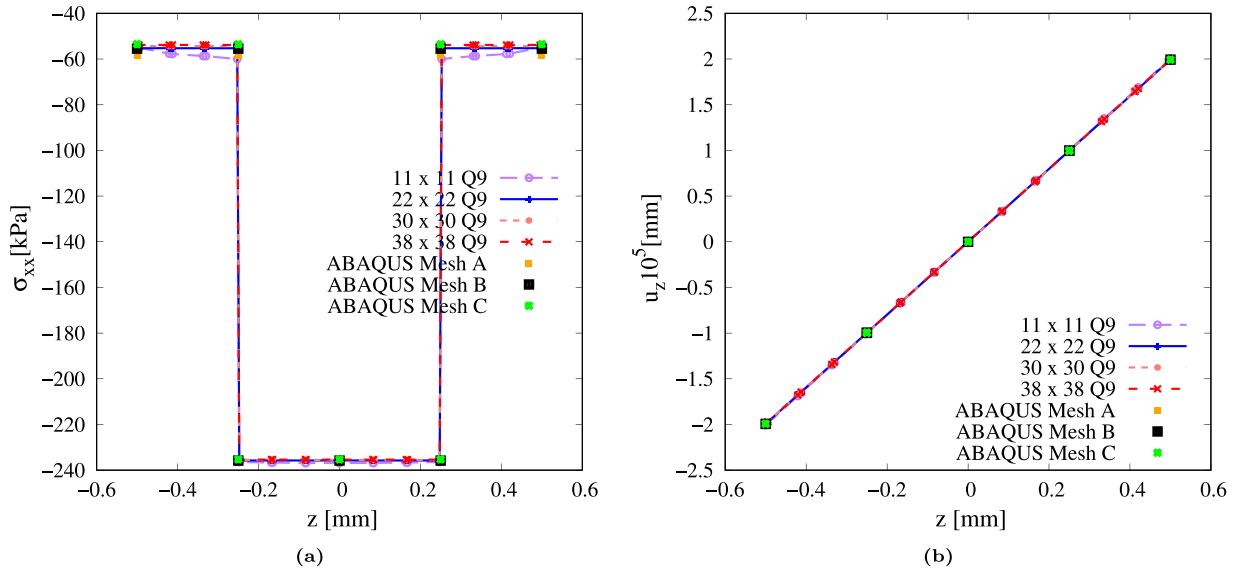
Fig. 5. Convergence study changing the number of Q9 elements with expansion theory 4LE3. ABAQUS 3D analyses is reported as a reference. [0/60/60/0] CFC plate with $\theta = 1°$ and camped. Results are taken at Point S. (a) σ_{xx}, (b) u_z.
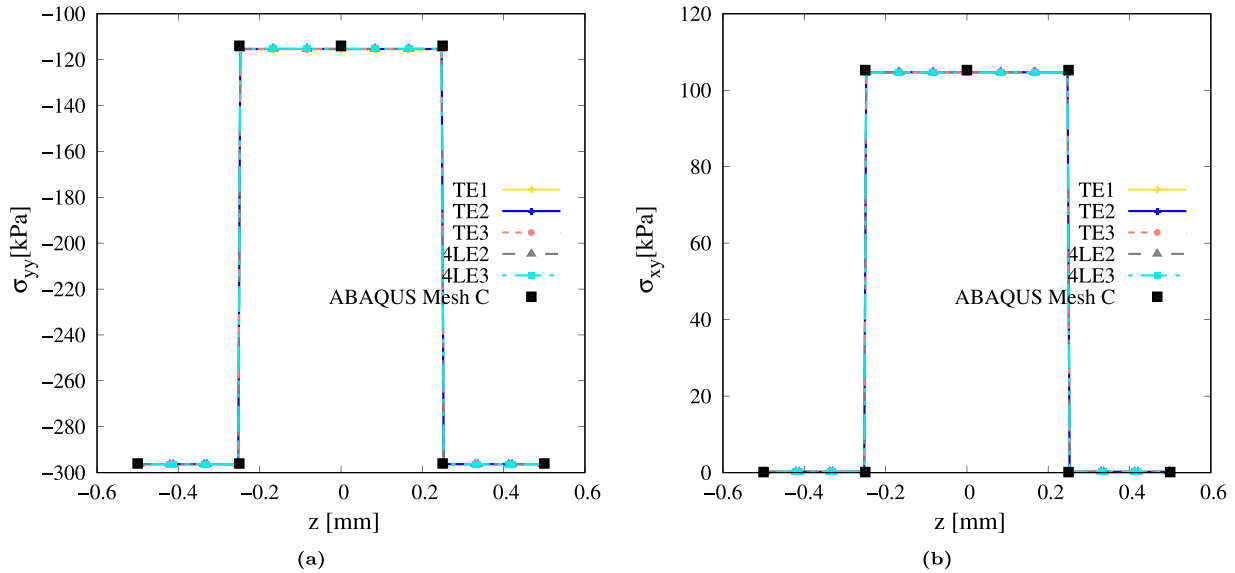

Fig. 6. Investigation of the expansion theory influence with 22×22 Q9 in-plane mesh. ABAQUS 3D analyses is reported as a reference. [0/60/60/0] CFC plate with $\theta = 1°$ and clamped edges. Results are taken at point S. (a) σ_{yy}, (b)σ_{xy}.

Table 5
Investigation of the expansion theory influences with 22×22 Q9 in-plane mesh, $\theta = 1°$. Results are taken at point S. $[0 < 90, 60 >, 0 < 45, 0 >]_s$ VAT plate composed of CFC. ABQ analysis with number of elements $62\,500$ C3D8R.

	Theory	$u_z \times 10^4$ [mm]	σ_{xx} [kPa]		σ_{yy} [kPa]		σ_{xy} [kPa]		DOF
		$z = \pm h/2$	$z = \pm h/2$	$z = 0$	$z = \pm h/2$	$z = 0$	$z = \pm h/2$	$z = 0$	
	ABQ C3D8R	± 0.1992	-279.89	-118.26	-51.70	-264.08	59.66	80.92	$238\,140$
CCCC	TE1	± 0.1993	-279.95	-93.76	-68.15	-261.10	60.97	83.90	$12\,150$
	4LE3	± 0.1993	-279.93	-93.70	-68.01	-261.08	61.00	83.92	$78\,975$
	TE1	± 0.1992	-279.34	-90.96	-64.23	-260.29	61.81	84.83	$12\,150$
	TE2	± 0.1994	-280.96	-96.53	-78.38	-262.34	58.46	82.85	$18\,225$
SSSS	TE3	± 0.1994	-280.98	-96.63	-78.59	-262.38	58.41	82.82	$24\,300$
	4LE2	± 0.2001	-285.21	-112.69	-111.58	-267.81	50.86	77.40	$54\,675$
	4LE3	± 0.2002	-285.32	-113.59	-111.79	-267.99	50.84	77.09	$78\,975$

All the in-plane and out-of-the-plane stresses are reported here. Due to the non-symmetric configuration of the stacking sequence, the plate bends, and the out-of-plane shear stresses arise along the thickness in both, simply supported and clamped configurations. Fig. 11 reports the phenomenology of the deflection in the 'z' direction, which is the most explicit representation of the difference due to the two BCs, as can also be seen in Table 6. In fact, for CCCC, the plate is constrained to not rotate near the boundary. For SSSS, there are four bending humps

Table 6
Investigation of the expansion theory influences with 22×22 Q9 in-plane mesh, $\theta = 1°$. Results are taken at point S. $[2(0 < 90, 60 >), 2(0 < 45, 0 >)]$ VAT GFRP plate.

	Theory	$u_z \times 10^4$ [mm]		σ_{xx} [kPa]		σ_{yy} [kPa]		σ_{xy} [kPa]	
		$z = -h/2$	$z = h/2$	$z = -h/2$	$z = h/2$	$z = -h/2$	$z = h/2$	$z = -h/2$	$z = h/2$
CCCC	TE1	−0.5190	0.1683	−284.19	−293.60	−286.58	−285.97	−1.109	−2.955
	4LE3	−0.5309	0.1563	−284.22	−293.43	−286.36	−285.88	−1.061	−2.914
SSSS	TE1	−0.2898	0.3974	−285.01	−291.09	−285.49	−285.21	−0.298	−2.452
	TE2	−0.2503	0.4376	−286.07	−294.58	−291.01	−286.14	−1.453	−3.635
	TE3	−0.2481	0.4399	−286.15	−294.85	−291.49	−286.23	−1.547	−3.722
	4LE2	−0.3329	0.3579	−289.60	−309.24	−309.41	−290.97	−5.209	−8.154
	4LE3	−0.3356	0.3553	−289.68	−309.58	−309.80	−291.09	−5.278	−8.250
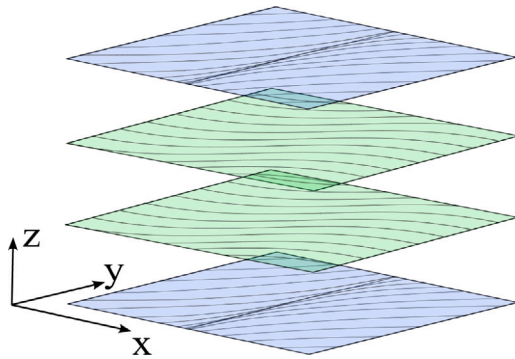
Fig. 7. VAT symmetric stacking sequence $[0 < 90, 60 >, 0 < 45, 0 >]_s$.

Table 7
Investigation of the expansion theory influences with 22×22 Q9 in-plane mesh, $\theta = 1°$. Results are taken at point S. $[2(0 < 90, 60 >), 2(0 < 45, 0 >)]$ VAT GFRP plate. Out of plane stresses.

	Theory	σ_{xz} [Pa]		σ_{yz} [Pa]	
		$z = -h/3$	$z = h/6$	$z = -h/3$	$z = h/6$
CCCC	TE1	−12.25	14.80	−250.67	−301.57
	TE2	−22.18	14.67	−283.37	279.92
	TE3	−13.63	10.83	−228.77	−406.15
	4LE2	−7.56	31.24	−201.95	−344.69
	4LE3	−6.88	35.45	−202.06	−343.50
SSSS	TE1	−108.91	−75.04	−101.59	−129.64
	TE2	−57.35	−84.01	−67.60	−125.26
	TE3	−49.15	−108.22	−36.20	−184.27
	4LE2	−12.11	−60.13	10.64	−108.63
	4LE3	−10.03	−59.42	14.02	−106.66

following the VAT lamination angle, and the plate is freer to deflect following the local fiber orientation. The displacement is represented in Fig. 11 from the top of the plate.

As evidenced by the results reported in Table 6, changing the expansion theory has only a minor impact on the in-plane stresses of CCCC BCs, which are more limited due to the constraints. On the other hand, SSSS plate presents fewer constraints at the boundary, and the influence of the expansion theory is more evident, as can be seen in Fig. 13. Nevertheless, σ_{xx} and σ_{yy} are comparable for the two BCs configurations in terms of trend and value.

Changing the adopted expansion thickness, the out-of-plane shear stresses reported in Figs. 12 and 13 show differences in trends and magnitude due to the bending. As expected, σ_{xz} and σ_{yz} appear to be continuous along the thickness using LE models, and an abrupt change in trend clearly represents the interface between the different orientations. Instead, TE models represent the interface between the two different orientations with a stress discontinuity.

The selected expansion theory strongly influences σ_{xz} and σ_{yz} in both constraint cases. In particular, the LW model employed in the LE theory only fulfills the boundary conditions. In the case of the TE model, even by increasing the degree of expansion, it is impossible to

fulfill the σ zero conditions in $z = \pm h/2$ and the necessary continuity of the out-of-plane stress. In both cases, the σ_{zz} stress is not represented because mechanical and thermal stresses offset each other, and the resultant σ_{zz} is zero. Fig. 13 clearly depicts the difference between the results obtained using different expansion theories, which also affects the trends of in-plane stress. The less accurate theories underestimate the in-plane stress, but the trend is respected in each analysis.

Fig. 14(a) reports displacement in $'z'$ direction for three different evaluation points, and their coordinates are presented in Fig. 14(b). The reported case is the SSSS GFRP plate. Due to the VAT deposition, the lamination angle changes along the plane of the plate as explained in Section 2, and the developed stresses and displacement will depend on the local lamination angle.

Despite being located at the center of the plate, the O point does not coincide with the point exhibiting the maximum displacement. It can be seen that point P has an almost entirely upward displacement, while in the case of point Q, the displacement is negative and directed downwards. The P and Q points are located in the two main deflections of the plate.

Fig. 15 depicts the shear stress σ_{yz} for four points calculated on a plate with 22×22 Q9 in-plane mesh and 4LE3 expansion theories. Symmetry in the stress trend is present. Furthermore, the values and the shapes of the stresses are influenced by the local lamination. As a result the shear stress is different when the lamination is different. On the other hand, the stresses are equal with opposite sign in the case of diagonal-symmetric points.

5. Discussion

Fig. 16 shows the relative difference between varying order theories of structures and the most accurate available LE3 model. The difference here is calculated considering Point S, where the stresses trends are reported in Figs. 8 and 9 for the symmetric CFC case and in Figs. 12 and 13 for the asymmetric GFRP plate. The selection of the stress to consider as the evaluation parameter depends on the considered analysis. σ_{yy} is assumed as reference parameter when the behavior of the symmetric plate composed of CFC is taken into account (Section 4.2). σ_{yz} is used for the graph in Fig. 16 for the GFRP asymmetric plate analyzed in Section 4.3 because, due to the bending, this plate develops shear stresses.

The percentage relative difference is calculated using the 2-norm of the stress values taken along the thickness. In Fig. 16, it is reported in a semi-logarithmic graph which allows some considerations about the choice of the adopted theory. The DOFs of the model are reported on the x-axis of the graph. For clarity, the bar below the graph in Fig. 16 depicts the corresponding adopted expansion theory. The LE3 model is taken as a reference result and, for this reason, is not reported. Through the evaluation of the trend, it can be noted that the BC influences most of the reach of the correct result. Although symmetric and asymmetric plates are compared, the curve that presents the same trend is the one with the same BCs. Therefore, using two different stresses as parameters do not influence the trends reported in the graph in Fig. 16. The selected stress parameter does not determine a significant difference
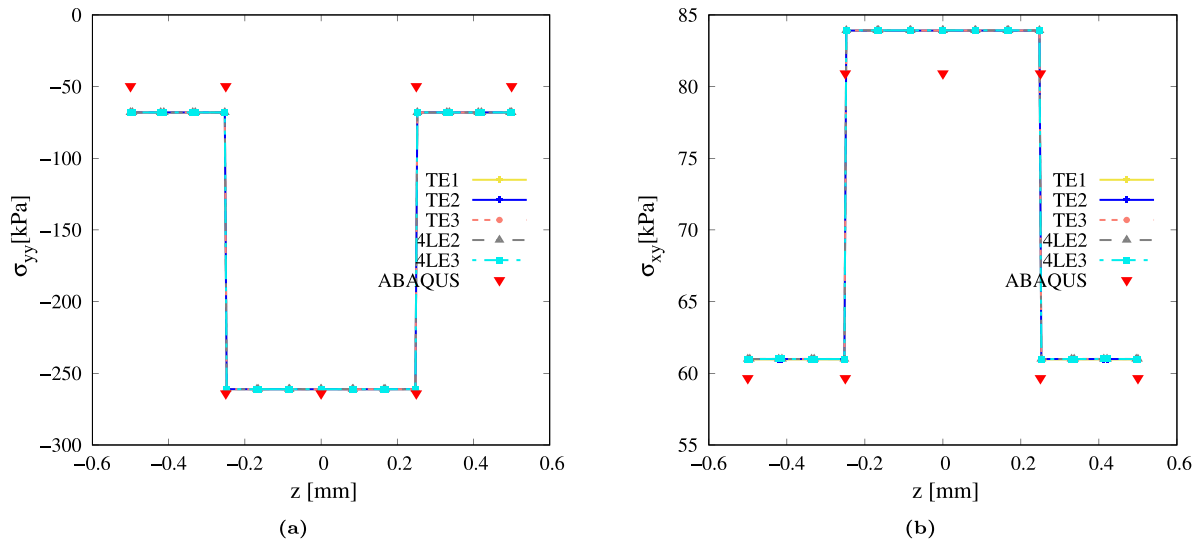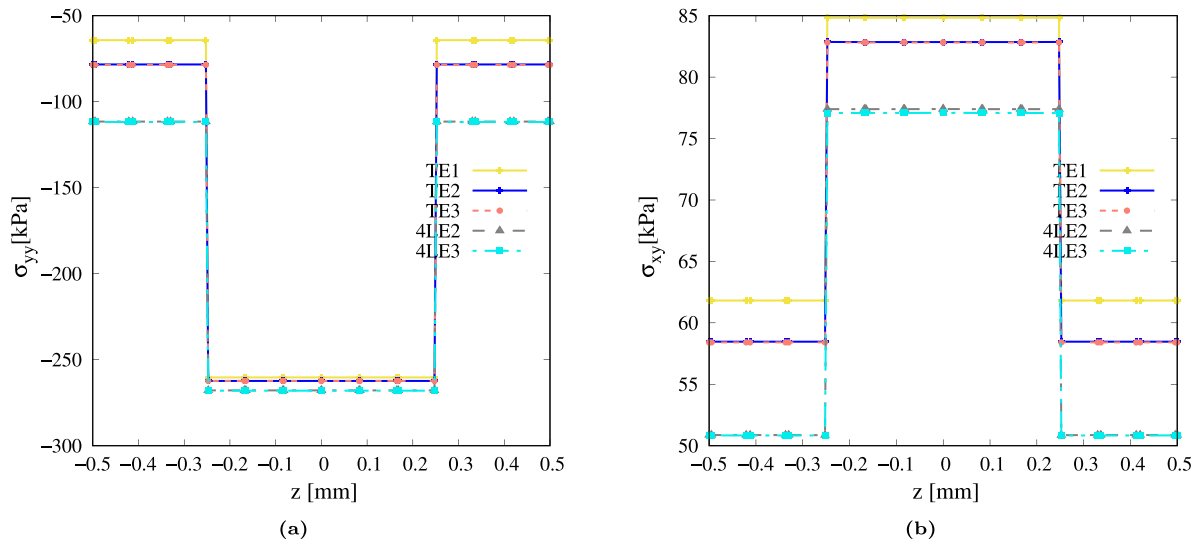
Fig. 8. Investigation of the expansion theory influences with 22 × 22 Q9 in-plane mesh, $\theta = 1°$. Results are taken at Point S. VAT $[0 < 90, 60 >, 0 < 45, 0 >]_s$ plate composed of CFC with clamped (CCCC) edges. (a) σ_{yy}, (b) σ_{xy}.

Fig. 9. Investigation of the expansion theory influences with 22 × 22 Q9 in-plane mesh, $\theta = 1°$. Results are taken at Point S. VAT $[0 < 90, 60 >, 0 < 45, 0 >]_s$ plate composed of CFC with simply supported (SSSS) edges. (a)σ_{yy}, (b) σ_{xy}.
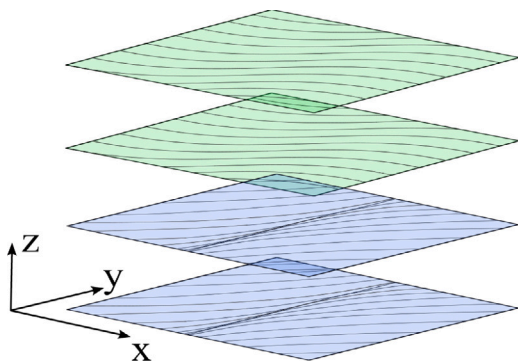
Fig. 10. VAT asymmetric stacking sequence $[2(0 < 90, 60 >), 2(0 < 45, 0 >)]$.

in the choice of the adequate expansion theory. As evident, the plates with clamped edges can be analyzed with the TE models without

any significant error in the results of stress value. LE models better represent the simply supported constraints, particularly for the GFRP asymmetric plate. The presented analyses apply a constant thermal profile as an external load. As demonstrated in [45], the external load greatly influences the plate's response behavior and the relative impact of the expansion theory.

6. Conclusions

This work employed the PVD within the CUF framework to describe the governing equation of the decoupled thermo-elastic problem for variable angle tow composite plates. The applied constant thermal profile made possible a simplified description of the phenomena without any dependence on the thickness coordinate. Furthermore, the unified formulation allows for a formal invariant modelization of the thermo-mechanical problem.

As an assessment, a numerical investigation was conducted on moderately thin plates with straight fiber deposition, comparing the results to ABAQUS simulations. The study focuses on Variable Angle
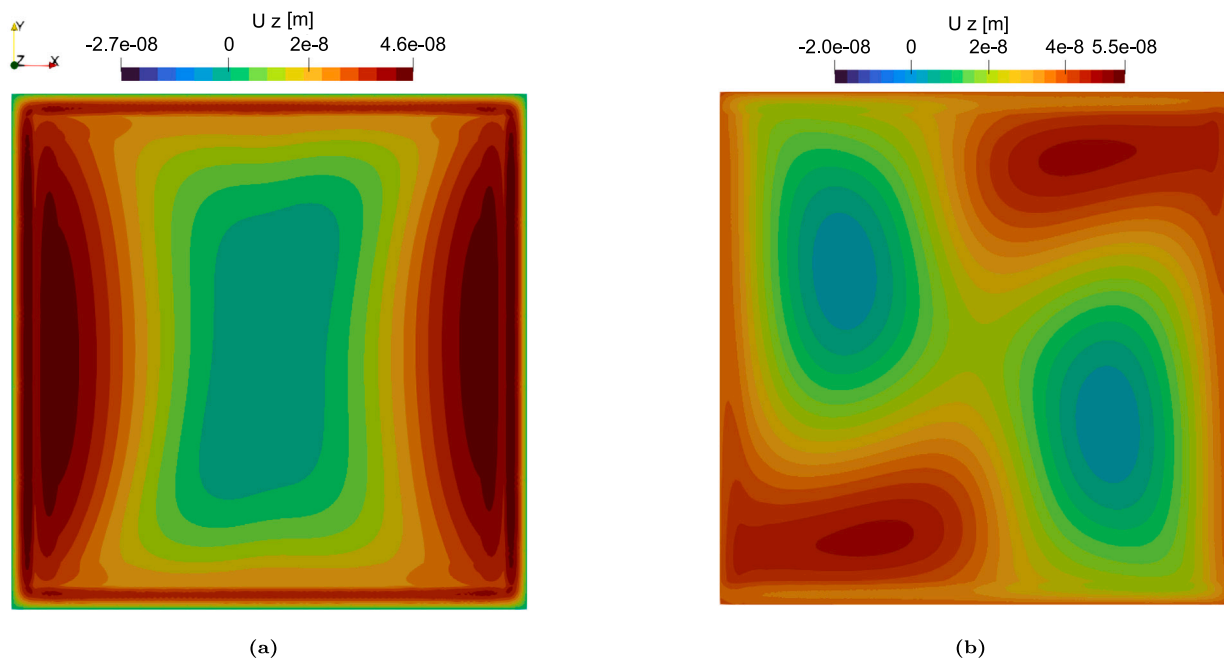
Fig. 11. Deflection in z direction. $[2(0 < 90, 60 >), 2(0 < 45, 0 >)]$ VAT plate composed of GFRP. (a) CCCC, (b) SSSS. Results reported from the top of the plate, discretization 22×22 Q9 4LE3 and $\theta = 1°$.

Tows (VAT) and examines symmetric and asymmetric plates under simply supported and clamped boundary conditions. The aim of the investigation is to report a representation of the along-the-thickness thermal stresses comparing different kinematic models. The influence of the along-the-thickness expansion theory is also investigated, and LE and TE models are compared for the different analyzed configurations.

- Symmetric plates subjected to a constant over-temperature throughout the thickness do not exhibit bending. As a consequence, the out-of-plane shear stresses are neglectable along the plate. On the other hand, in an asymmetric plate, the coupling between out-of-plane and in-plane behaviors causes a rise in out-of-plane shear stresses that are no longer neglectable.
- The results show that the LE models fulfill continuity requirements of the out-of-plane shear stresses at the interface and respect the zero conditions at plate boundaries for the same stress trends. On the other hand, the TE models do not reach zero values for out-of-plane shear stress at the plate boundaries, and they display a discontinuity at the layer interface.
- Due to the constant applied load, away from the boundaries σ_{zz} is null as the mechanic and thermal components offset each other.
- The boundary conditions greatly influence the selection of the adequate expansion theory. For simply supported cases, the LE models present better results in terms of stress value with a satisfactory trend for every case. However, the clamped configuration can also be described from TE models without significant stress-value errors.

Future analyses should address problems related to thick plates where the shear influence increases. Asymmetric configurations with a greater number of different layers could also be investigated. Additionally, considering more complex thermal profile influences could further enhance the understanding of the thermo-elastic behavior.

CRediT authorship contribution statement

A. Pagani: Conceptualization, Resources, Writing – review & editing, Supervision, Project administration, Funding acquisition. **E. Zappino:** Conceptualization, Methodology, Software, Supervision. **F. Bracaglia:** Methodology, Validation, Formal analysis, Investigation, Writing – original draft, Visualization. **R. Masia:** Software, Formal analysis, Writing – original draft, Visualization. **E. Carrera:** Conceptualization, Supervision, Project administration.

Declaration of competing interest

The authors declare that they have no known competing financial interests or personal relationships that could have appeared to influence the work reported in this paper.

Data availability

Data will be made available on request.

Appendix A. Geometrical relation

The linear differential operator b allows to describe the relation between the displacement u and the strain ϵ.

$$b = \begin{pmatrix} \frac{\partial}{\partial x} & 0 & 0 \\ 0 & \frac{\partial}{\partial y} & 0 \\ 0 & 0 & \frac{\partial}{\partial z} \\ \frac{\partial}{\partial z} & 0 & \frac{\partial}{\partial x} \\ 0 & \frac{\partial}{\partial z} & \frac{\partial}{\partial y} \\ \frac{\partial}{\partial y} & \frac{\partial}{\partial x} & 0 \end{pmatrix} \qquad (20)$$
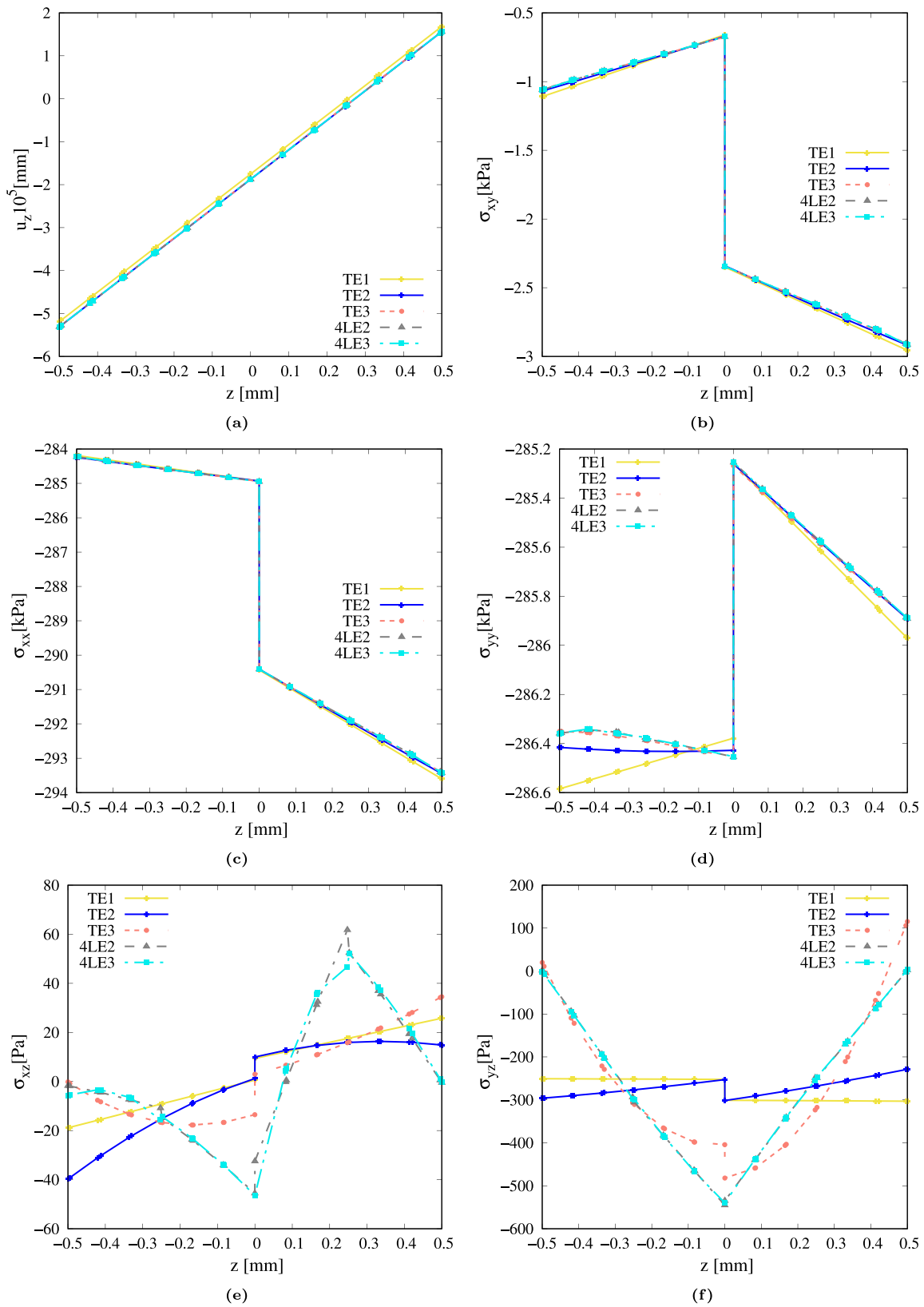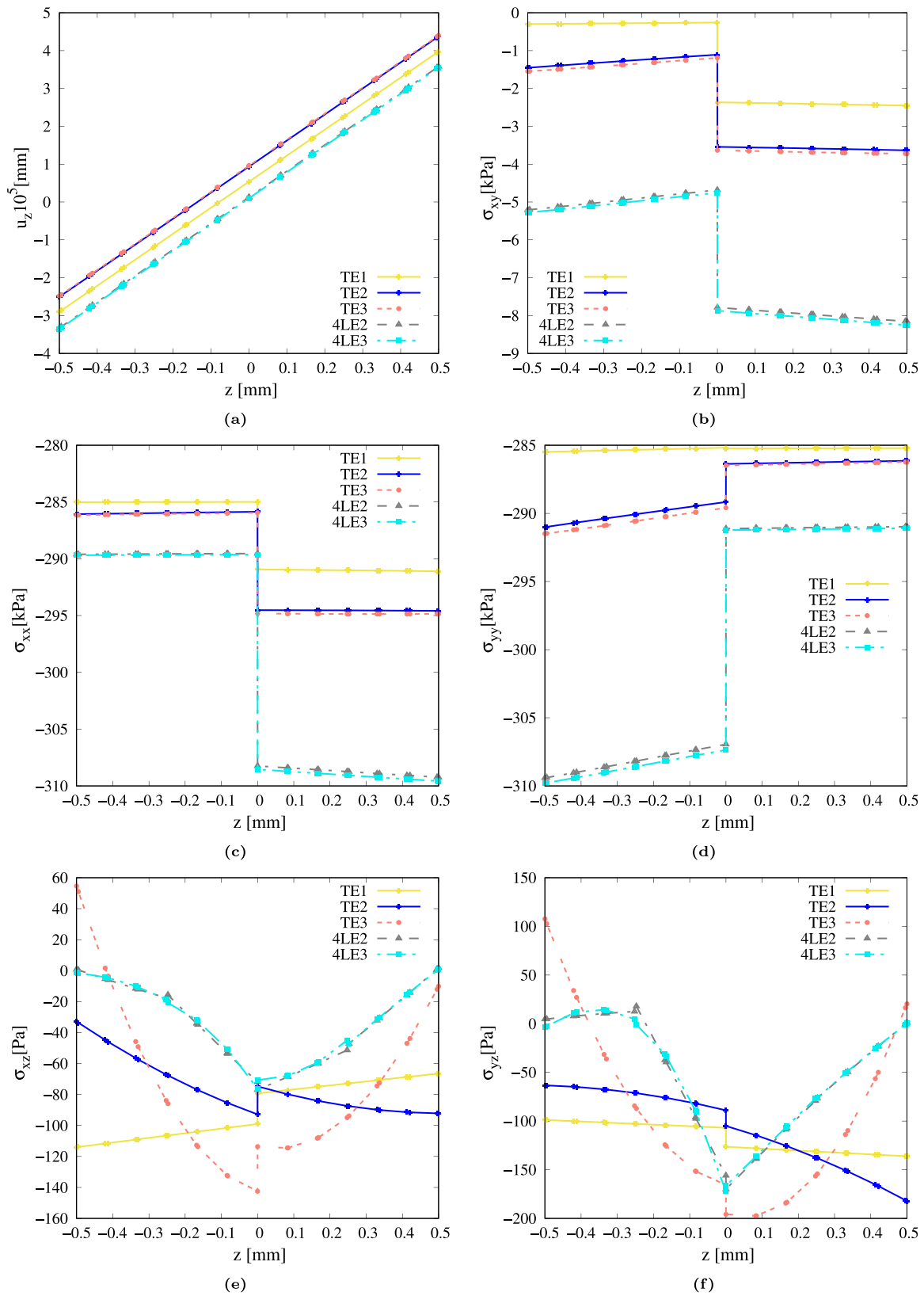
Fig. 12. Investigation of the expansion theory influences with 22×22 Q9 in-plane mesh, $\theta = 1°$. Results are taken at point S. $[2(0 < 90, 60 >), 2(0 < 45, 0 >)]$ VAT plate composed of GFRP. CCCC constraint. (a) u_z, (b) σ_{xy}, (c) σ_{xx}, (d) σ_{yy}, (e) σ_{xz}, (f) σ_{yz}.

Fig. 13. Investigation of the expansion theory influences with 22×22 Q9 in-plane mesh, $\theta = 1°$. Results are taken at point S. $[2(0 < 90, 60 >), 2(0 < 45, 0 >)]$ VAT plate composed of GFRP. SSSS constraint. (a) u_z, (b) σ_{xy},(c) σ_{xx}, (d) σ_{yy},(e) σ_{xz},(f) σ_{yz}.
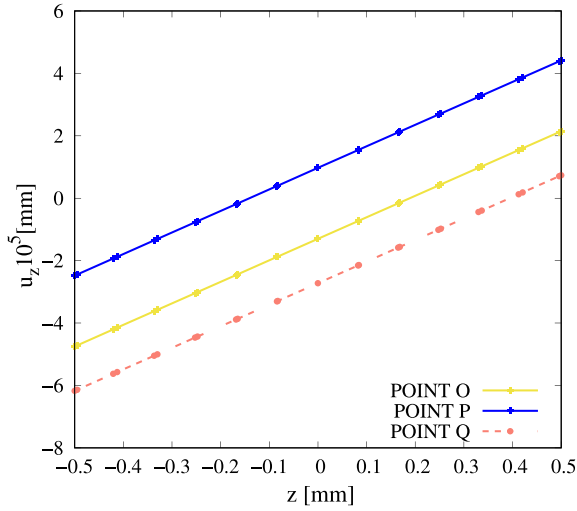
(a) u_z along the thickness.
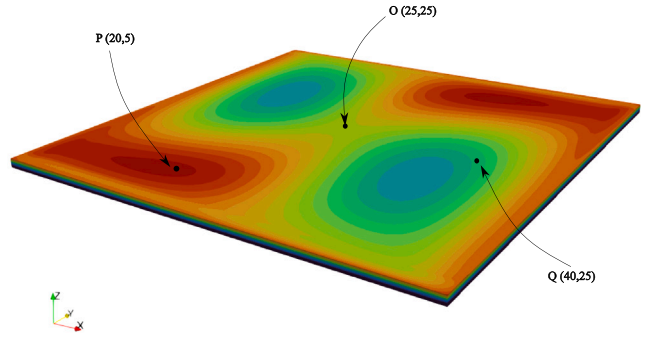
(b) Points where magnitude are measured $[mm]$. u_z contour plot.

Fig. 14. u_z, lamination $[2(0 < 90, 60 >), 2(0 < 45, 0 >)]$ VAT GFRP SSSS plate. 22×22 Q9, 4LE3, $\theta = 1°$.
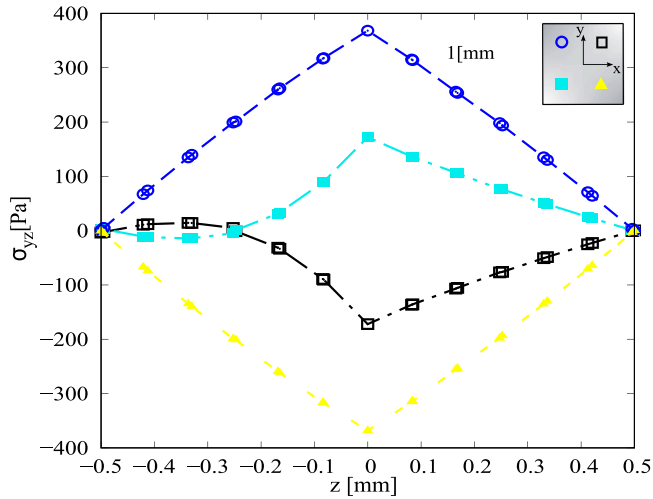

Fig. 15. σ_{yz} calculated in four points in the quarters of the plate. 22×22 Q9, 4LE3. $\theta = 1°$, simply supported GFRP VAT plate $[2(0 < 90, 60 >), 2(0 < 45, 0 >)]$.
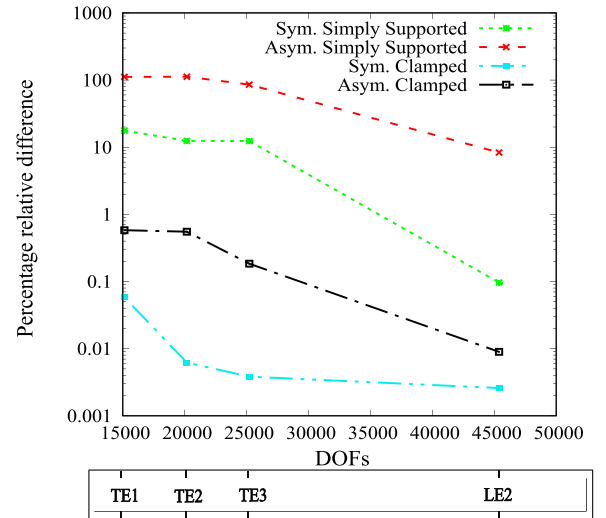

Fig. 16. Investigation of the adequate expansion theory expressed by percentage relative distance calculated to LE3 results. Semi-logarithmic representation. Results taken at Point S, in-plane mesh 22×22.

Appendix B. Fundamental nucleus

The CUF mechanical fundamental nuclei are reported below, where the material coefficients depend on the local fiber orientation and are expressed in the local reference system.

$$K_{xx}^{\tau sij} = \int_{\Omega} C_{11} N_{i,x} N_{j,x} d\Omega \int_h F_\tau F_s dz$$
$$+ \int_{\Omega} C_{16} N_{i,x} N_{j,y} d\Omega \int_h F_\tau F_s dz$$
$$+ \int_{\Omega} C_{16} N_{i,y} N_{j,x} d\Omega \int_h F_\tau F_s dz \quad + \quad \int_{\Omega} C_{44} N_i N_j d\Omega$$
$$\times \int_h F_{\tau,z} F_{s,z} dz \quad + \quad \int_{\Omega} C_{66} N_{i,y} N_{j,y} d\Omega \int_h F_\tau F_s dz \quad (21)$$

$$K_{xy}^{\tau sij} = \int_{\Omega} C_{12} N_{i,y} N_{j,x} d\Omega \int_h F_\tau F_s dz$$
$$+ \int_{\Omega} C_{62} N_{i,y} N_{j,y} d\Omega \int_h F_\tau F_s dz$$
$$+ \int_{\Omega} C_{16} N_{i,x} N_{j,x} d\Omega \int_h F_\tau F_s dz \quad + \quad \int_{\Omega} C_{45} N_i N_j d\Omega$$

$$\times \int_h F_{\tau,z} F_{s,z} dz \quad + \quad \int_{\Omega} C_{66} N_{i,x} N_{j,y} d\Omega \int_h F_\tau F_s dz \quad (22)$$

$$K_{xz}^{\tau sij} = \int_{\Omega} C_{13} N_i N_{j,x} d\Omega \int_h F_{\tau,z} F_s dz$$
$$+ \int_{\Omega} C_{63} N_i N_{j,y} d\Omega \int_h F_{\tau,z} F_s dz$$
$$+ \int_{\Omega} C_{44} N_{i,x} N_j d\Omega \int_h F_\tau F_{s,z} dz$$
$$+ \int_{\Omega} C_{45} N_{i,y} N_j d\Omega \int_h F_\tau F_{s,z} dz \quad (23)$$

$$K_{yx}^{\tau sij} = \int_{\Omega} C_{21} N_{i,x} N_{j,y} d\Omega \int_h F_\tau F_s dz$$
$$+ \int_{\Omega} C_{61} N_{i,x} N_{j,x} d\Omega \int_h F_\tau F_s dz$$
$$+ \int_{\Omega} C_{26} N_{i,y} N_{j,y} d\Omega \int_h F_\tau F_s dz \quad + \quad \int_{\Omega} C_{45} N_i N_j d\Omega$$
$$\times \int_h F_{\tau,z} F_{s,z} dz \quad + \quad \int_{\Omega} C_{66} N_{i,y} N_{j,x} d\Omega \int_h F_\tau F_s dz \quad (24)$$

$$K_{yy}^{\tau s i j} = \int_\Omega C_{22} N_{i,y} N_{j,y} d\Omega \int_h F_\tau F_s dz$$
$$+ \int_\Omega C_{62} N_{i,y} N_{j,x} d\Omega \int_h F_\tau F_s dz$$
$$+ \int_\Omega C_{26} N_{i,x} N_{j,y} d\Omega \int_h F_\tau F_s dz \; + \; \int_\Omega C_{55} N_i N_j d\Omega$$
$$\times \int_h F_{\tau,z} F_{s,z} dz \; + \; \int_\Omega C_{66} N_{i,x} N_{j,x} d\Omega \int_h F_\tau F_s dz \tag{25}$$

$$K_{yz}^{\tau s i j} = \int_\Omega C_{23} N_i N_{j,y} d\Omega \int_h F_{\tau,z} F_s dz$$
$$+ \int_\Omega C_{63} N_i N_{j,x} d\Omega \int_h F_{\tau,z} F_s dz$$
$$+ \int_\Omega C_{55} N_{i,y} N_j d\Omega \int_h F_\tau F_{s,z} dz$$
$$+ \int_\Omega C_{45} N_{i,x} N_j d\Omega \int_h F_\tau F_{s,z} dz \tag{26}$$

$$K_{zx}^{\tau s i j} = \int_\Omega C_{31} N_{i,x} N_j d\Omega \int_h F_\tau F_{s,z} dz$$
$$+ \int_\Omega C_{44} N_i N_{j,x} d\Omega \int_h F_{\tau,z} F_s dz$$
$$+ \int_\Omega C_{45} N_i N_{j,y} d\Omega \int_h F_{\tau,z} F_s dz$$
$$+ \int_\Omega C_{36} N_{i,y} N_j d\Omega \int_h F_\tau F_{s,z} dz \tag{27}$$

$$K_{zy}^{\tau s i j} = \int_\Omega C_{32} N_{i,y} N_j d\Omega \int_h F_\tau F_{s,z} dz$$
$$+ \int_\Omega C_{55} N_i N_{j,y} d\Omega \int_h F_{\tau,z} F_s dz$$
$$+ \int_\Omega C_{45} N_i N_{j,x} d\Omega \int_h F_{\tau,z} F_s dz$$
$$+ \int_\Omega C_{36} N_{i,x} N_j d\Omega \int_h F_\tau F_{s,z} dz \tag{28}$$

$$K_{zz}^{\tau s i j} = \int_\Omega C_{33} N_i N_j d\Omega \int_h F_{\tau,z} F_{s,z} dz$$
$$+ \int_\Omega C_{44} N_{i,x} N_{j,x} d\Omega \int_h F_\tau F_s dz$$
$$+ \int_\Omega C_{45} N_{i,x} N_{j,y} d\Omega \int_h F_\tau F_s dz \; + \; \int_\Omega C_{45} N_{i,y} N_{j,x} d\Omega$$
$$\times \int_h F_\tau F_s dz \; + \; \int_\Omega C_{55} N_{i,y} N_{j,y} d\Omega \int_h F_\tau F_s dz \tag{29}$$

Following, the explicit terms of the fundamental nucleus of the thermal load matrix are reported for the case of constant thermal load $\theta(z) = \theta$.

$$\Theta_1 = \theta \int_\Omega \lambda_1 N_{j,x} d\Omega \int_h F_s dz + \theta \int_\Omega \lambda_{12} N_{j,y} d\Omega \int_h F_s dz \tag{30}$$

$$\Theta_2 = \theta \int_\Omega \lambda_2 N_{j,y} d\Omega \int_h F_s dz + \theta \int_\Omega \lambda_{12} N_{j,x} d\Omega \int_h F_s dz \tag{31}$$

$$\Theta_3 = \theta \int_\Omega \lambda_3 N_j d\Omega \int_h F_{s,z} dz \tag{32}$$

References

[1] Kapania RK. A review on the analysis of laminated shells. 1989.

[2] Oromiehie E, Prusty BG, Compston P, Rajan G. Automated fibre placement based composite structures: Review on the defects, impacts and inspections techniques. Compos Struct 2019;224:110987.

[3] Kim BC, Weaver PM, Potter K. Computer aided modelling of variable angle tow composites manufactured by continuous tow shearing. Compos Struct 2015;129:256–67.

[4] Hyer MW, Charette RF. Use of curvilinear fiber format in composite structure design. AIAA J 1991;29(6):1011–5.

[5] Demasi L, Biagini G, Vannucci F, Santarpia E, Cavallaro R. Equivalent single layer, zig-zag, and layer wise theories for variable angle tow composites based on the generalized unified formulation. Compos Struct 2017;177:54–79.

[6] Patni M, Minera S, Groh RMJ, Pirrera A, Weaver PM. On the accuracy of localised 3D stress fields in tow-steered laminated composite structures. Compos Struct 2019;225:111034.

[7] Zhu Y, Qin Y, Qi S, Xu H, Liu D, Yan C. Variable angle tow reinforcement design for locally reinforcing an open-hole composite plate. Compos Struct 2018;202:162–9.

[8] Wu Z, Weaver PM, Raju G, Kim BC. Buckling analysis and optimisation of variable angle tow composite plates. Thin-Wall Struct 2012;60:163–72.

[9] Vescovini Riccardo, Dozio Lorenzo. A variable-kinematic model for variable stiffness plates: Vibration and buckling analysis. Compos Struct 2016;142:15–26.

[10] Sánchez-Majano AR, Pagani A. Buckling and fundamental frequency optimization of tow-steered composites using layerwise structural models. AIAA J 2023;1–15.

[11] Groh RMJ, Weaver PM. Deleterious localized stress fields: the effects of boundaries and stiffness tailoring in anisotropic laminated plates. Proc R Soc Lond Ser A: Math Phys Eng Sci 2016;472(2194):20160391.

[12] Pagani A, Sanchez-Majano AR. Stochastic stress analysis and failure onset of variable angle tow laminates affected by spatial fibre variations. Composites C 2021;4:100091.

[13] Pagani A, Sanchez-Majano AR. Influence of fiber misalignments on buckling performance of variable stiffness composites using layerwise models and random fields. Mech Adv Mater Struct 2022;29(3):384–99.

[14] Sanchez-Majano AR, Pagani A, Petrolo M, Zhang C. Buckling sensitivity of tow-steered plates subjected to multiscale defects by high-order finite elements and polynomial chaos expansion. Materials 2021;14(11):2706.

[15] Stodieck Olivia, Cooper Jonathan E, Weaver Paul M, Kealy Paul. Improved aeroelastic tailoring using tow-steered composites. Compos Struct 2013;106:703–15.

[16] Brooks TR, Martins JRRA, Kennedy GJ. Aerostructural tradeoffs for tow-steered composite wings. J Aircr 2020;57(5):787–99.

[17] Duran AV, Fasanella NA, Sundararaghavan V, Waas AM. Thermal buckling of composite plates with spatial varying fiber orientations. Compos Struct 2015;124:228–35.

[18] Vescovini R, Dozio L. Thermal buckling behaviour of thin and thick variable-stiffness panels. J Compos Sci 2018;2(4):58.

[19] Bhaskar K, Varadan TK, Ali JSM. Thermoelastic solutions for orthotropic and anisotropic composite laminates. Composites B 1996;27(5):415–20.

[20] Tungikar VB, Rao KM. Three dimensional exact solution of thermal stresses in rectangular composite laminate. Compos Struct 1994;27(4):419–30.

[21] Azzara R, Carrera E, Filippi M, Pagani A. Vibration analysis of thermally loaded isotropic and composite beam and plate structures. J Therm Stress 2023;46(5):369–86.

[22] Fazzolari FA. Natural frequencies and critical temperatures of functionally graded sandwich plates subjected to uniform and non-uniform temperature distributions. Compos Struct 2015;121:197–210.

[23] Thornton EA. Thermal buckling of plates and shells. 1993.

[24] Kant T, Khare RK. Finite element thermal stress analysis of composite laminates using a higher-order theory. J Therm Stress 1994;17(2):229–55.

[25] Rolfes R, Noor AK, Sparr H. Evaluation of transverse thermal stresses in composite plates based on first-order shear deformation theory. Comput Methods Appl Mech Engrg 1998;167(3–4):355–68.

[26] Wu Z, Chen W. A global-local higher order theory for multilayered shells and the analysis of laminated cylindrical shell panels. Compos Struct 2008;84(4):350–61.

[27] Jang-Woo H, Jun-Sik K, Maenghyo C. New enhanced first-order shear deformation theory for thermo-mechanical analysis of laminated composite and sandwich plates. Composites B 2017;116:422–50.

[28] Carrera E. Temperature profile influence on layered plates response considering classical and advanced theories. AIAA J AIAA J 2002;40:1885–96.

[29] Carrera E, Cinefra M, Fazzolari FA. Some results on thermal stress of layered plates and shells by using unified formulation. J Therm Stress 2013;36(6):589–625.

[30] Cinefra M, Valvano S, Carrera E. Heat conduction and thermal stress analysis of laminated composites by a variable kinematic MITC9 shell element. Curved Layer Struct 2015;2(1).

[31] Entezari A, Filippi M, Carrera E. Unified finite element approach for generalized coupled thermoelastic analysis of 3D beam-type structures, part 1: Equations and formulation. J Therm Stress 2017;40(11):1386–401.

[32] Carrera E, Valvano S. A variable kinematic shell formulation applied to thermal stress of laminated structures. J Therm Stress 2017;40(7):803–27.

[33] Carrera Erasmo. Historical review of zig-zag theories for multilayered plates and shells. Appl Mech Rev 2003;56(3):287–308.

[34] Reddy JN. An evaluation of equivalent-single-layer and layerwise theories of composite laminates. Compos Struct 1993;25(1–4):21–35.

[35] Murakami H. Laminated composite plate theory with improved in-plane responses. 1986.

[36] Sánchez-Majano AR, Azzara R, Pagani A, Carrera E. Accurate stress analysis of variable angle tow shells by high-order equivalent-single-layer and layer-wise finite element models. Materials 2021;14(21).

[37] Milazzo A. Layer-wise and equivalent single layer models for smart multilayered plates. Composites B 2014;67:62–75.

[38] Heinecke F, Willberg C. Manufacturing-induced imperfections in composite parts manufactured via automated fiber placement. J Compos Sci 2019;3(2):56.

[39] Gurdal Z, Olmedo R. In-plane response of laminates with spatially varying fiber orientations-variable stiffness concept. AIAA J 1993;31(4):751–8.

[40] Viglietti A, Zappino E, Carrera E. Analysis of variable angle tow composites structures using variable kinematic models. Composites B 2019;171. http://dx. doi.org/10.1016/j.compositesb.2019.03.072.

[41] Pagani A, Carrera E, Augello R, Scano D. Use of Lagrange polynomials to build refined theories for laminated beams, plates and shells. Compos Struct 2021;276:114505.

[42] Reddy JN. Mechanics of laminated composite plates and shells: theory and analysis. CRC Press; 2003.

[43] Carrera E, Cinefra M, Petrolo M, Zappino E. Finite element analysis of structures through unified formulation. John Wiley & Sons; 2014, in press.

[44] Carrera E, Petrolo M. Guidelines and recommendations to construct theories for metallic and composite plates. AIAA J 2010;48(12):2852–66.

[45] Carrera E. An assessment of mixed and classical theories for the thermal stress analysis of orthotropic multilayered plates. J Therm Stress 2000;23(9):797–831.